

Retained strength of UHTCMCs after oxidation at 2278 K

*Original*

Retained strength of UHTCMCs after oxidation at 2278 K / Galizia, P.; Vinci, A.; Zoli, L.; Monteverde, F.; Binner, J.; Venkatachalam, V.; Lagos, M. A.; Reimer, T.; Jain, N.; Sciti, D.. - In: COMPOSITES. PART A: APPLIED SCIENCE AND MANUFACTURING. - ISSN 1359-835X. - ELETTRONICO. - 149:(2021), p. 106523.  
[10.1016/j.compositesa.2021.106523]

*Availability:*

This version is available at: 11583/2948334 since: 2022-01-21T10:25:22Z

*Publisher:*

Elsevier Ltd

*Published*

DOI:10.1016/j.compositesa.2021.106523

*Terms of use:*

This article is made available under terms and conditions as specified in the corresponding bibliographic description in the repository

*Publisher copyright*

Elsevier postprint/Author's Accepted Manuscript

© 2021. This manuscript version is made available under the CC-BY-NC-ND 4.0 license  
<http://creativecommons.org/licenses/by-nc-nd/4.0/>. The final authenticated version is available online at:  
<http://dx.doi.org/10.1016/j.compositesa.2021.106523>

(Article begins on next page)

# Composites Part A

## Retained strength of UHTCMCs after oxidation at 2278 K

--Manuscript Draft--

<b>Manuscript Number:</b>	JCOMA-20-2766R1
<b>Article Type:</b>	Research Paper
<b>Keywords:</b>	A. Ceramic-matrix composites (CMCs); B. Cure behaviour; B. Environmental degradation; D. Mechanical testing
<b>Corresponding Author:</b>	Antonio Vinci Institute of Science and Technology for Ceramics Faenza, ITALY
<b>First Author:</b>	Pietro Galizia
<b>Order of Authors:</b>	Pietro Galizia
	Antonio Vinci
	Luca Zoli
	Frederic Monteverde
	Jon Binner
	Vinothini Venkatachalam
	Miguel. A. Lagos
	Thomas Reimer
	Neraj Jain
<b>Manuscript Region of Origin:</b>	Diletta Sciti
	ITALY
<b>Abstract:</b>	In the frame of Horizon 2020 European C3HARME research project, the manufacture of ZrB <sub>2</sub> -based CMCs was developed through different processes: slurry infiltration and sintering, radio frequency chemical vapour infiltration (RF-CVI) and reactive metal infiltration (RMI). To assess the high temperature stability, room temperature bending strength was measured after oxidizing the samples at 2278 K and compared to the strength of the as-produced materials. Microstructures were analysed before and after the thermal treatment to assess the damage induced by the high temperature oxidation. Short fibre-reinforced composites showed the highest retained strength (>80%) and an unchanged stress-strain curve.
<b>Response to Reviewers:</b>	<p>Dear Editor, we wish to thank you and the reviewers for your feedback and time. We have addressed every reviewer's comment below. Changes will be highlighted in blue.</p> <p>Editor/referees' comments:</p> <p>Reviewer #1: This manuscript reports new findings of the strength of UHTCMCs after high temperature oxidation. There are indeed novel reports with rigorous analysis that would be of interest to the journal audience. It is recommended for publication with minor revisions based on specific questions and comments below that should be integrated into the manuscript.</p> <p>1. Abstract- Spell out the C3HARME acronym - Originally we had spelled out the acronym like we did in the introduction, but that alone took over 10 words (10% of the allowance for the abstract), and so we opted out for a shortened version, preferring to report more results instead.</p> <p>2. Introduction - More information/motivation/context of UHTCMCs is needed in the introduction for this journal audience. Especially information on how this work fills a gap in the reported literature in the area. There is no mention in the introduction on the materials of interest (namely Cf reinforcements into Zr-rich matrix) and test procedure</p>

## Retained strength of UHTCMCs after oxidation at 2278 K

Pietro Galizia<sup>1</sup>, Antonio Vinci<sup>1\*</sup>, Luca Zoli<sup>1</sup>, Frederic Monteverde<sup>1</sup>, Jon Binner<sup>2</sup>, Vinothini Venkatachalam<sup>2</sup>, Miguel. A. Lagos<sup>3</sup>, Thomas Reimer<sup>4</sup>, Neraj Jain<sup>4</sup>, Diletta Sciti<sup>1</sup>

\* Corresponding author

<sup>1</sup> CNR-ISTEC, National Research Council of Italy, Institute of Science and Technology for Ceramics, Via Granarolo, Faenza (RA), 64-48018, Italy

<sup>2</sup> School of Metallurgy and Materials - University of Birmingham, Birmingham B15 2TT, UK

<sup>3</sup> TECNALIA, Basque Research and Technology Alliance (BRTA), Mikeletegi Pasealekua 2, 20009 Donostia-San Sebastián, Spain

<sup>4</sup> DLR German Aerospace Center, Institute of Structures and Design, Pfaffenwaldring 38-40, 70569 Stuttgart, Germany

### Abstract

In the frame of Horizon 2020 European C<sup>3</sup>HARME research project, the manufacture of ZrB<sub>2</sub>-based CMCs was developed through different processes: slurry infiltration and sintering, radio frequency chemical vapour infiltration (RF-CVI) and reactive metal infiltration (RMI). To assess the high temperature stability, room temperature bending strength was measured after oxidizing the samples at 2278 K and compared to the strength of the as-produced materials. Microstructures were analysed before and after the thermal treatment to assess the damage induced by the high temperature oxidation. Short fibre-reinforced composites showed the highest retained strength (>80 %) and an unchanged stress-strain curve.

**Keywords:** A. Ceramic-matrix composites (CMCs); B. Cure behaviour; B. Environmental degradation; D. Mechanical testing

### 1 Introduction

A novel class of ultra-high temperature (UHT) ceramic-matrix composites (CMCs), progressively recognized as UHTCMCs, is currently under extensive study within the Horizon 2020 European C<sup>3</sup>HARME research project [1,2]. The C<sup>3</sup>HARME acronym stands for Next Generation Ceramic Composites for Harsh Combustion Environment and Space. In fact, the main application field of UHTCMCs developed in C<sup>3</sup>HARME research project is aerospace, in particular new technological

After injection, the preforms containing about 29%  $\text{ZrB}_2$  were cleaned and dried in an air oven and further densified with pyrolytic carbon using a radio frequency (RF) heated chemical vapour infiltration process (RF-CVI), reaching the final nominal composition reported in Table 1. *CVI-2*: This composite is a variant of *CVI-1*, where the injected slurry had a different composition, namely 15 vol.%  $\text{ZrB}_2$  + 10 vol.%  $\text{SiC}$  + 5 vol.%  $\text{Y}_2\text{O}_3$ , using  $\text{SiC}$  and  $\text{Y}_2\text{O}_3$  nanopowders. The preform was again subsequently densified by the RF-CVI process, reaching the final nominal composition reported in Table 1.

Finally, the last 2 composites were obtained by the reactive metal infiltration process (RMI). *RMI-1 and 2*: Both samples were manufactured using UF-XN80-300 unidirectional laminates with uncoated fibres. The initial fibre volume content was 38 vol.% but decreased to around 30 vol.% due to increasing thickness during infiltration [25]. The laminates were impregnated with a phenolic-based slurry containing a powder mixture of elemental B and  $\text{ZrB}_2$  before stacking in a 0/90° configuration and curing at 423 K. After pyrolysis, the porous matrix contained B, C and  $\text{ZrB}_2$  phases. The porous samples were then infiltrated with  $\text{B}_2\text{O}_3$  in order to transform the porous carbon from the phenolic into  $\text{B}_4\text{C}$  for infiltration. Material *RMI-1* was infiltrated with liquid Zr 706 (2173 K) whilst material *RMI-2* with  $\text{Zr}_2\text{Cu}$ -1% B was infiltrated at 1473 K.

**Table 1.** Green preparation method, consolidation techniques, type of fibre preform, compositions expressed as volumetric amount of the ceramic phases measured by image analysis and porosity, and measured geometrical density ( $\rho$ ).

Sample	Green preparation	Consolidation technique	Fibre preform	Composition	P	$\rho$
				vol. %	vol. %	$\text{g/cm}^3$
CFHP	Fibre mixing	HP	Chopped fibres	52 $\text{ZrB}_2$ +3 $\text{SiC}$ +38 $\text{C}_f$	7	4.3
MFSPS		SPS	Milled fibres	49 $\text{ZrB}_2$ +10 $\text{SiC}$ +40 $\text{C}_f$	1	4.1
SIHP-1	Slurry impregnation	HP	UD fibre sheet	48 $\text{ZrB}_2$ +3 $\text{SiC}$ +47 $\text{C}_f$	2	4.2
SIHP-2				46 $\text{ZrB}_2$ +5 $\text{SiC}$ +48 $\text{C}_f$	1	4.1
CVI-1	Slurry impregnation	RF-CVI	2.5D preform	28 $\text{ZrB}_2$ +23 $\text{C}_f$ +46PyC	3	3.1
CVI-2				15 $\text{ZrB}_2$ +10 $\text{SiC}$ +5 $\text{Y}_2\text{O}_3$ +23 $\text{C}_f$ +37PyC	10	2.7
RMI-1	Slurry impregnation	RMI	UD fibre sheet	66( $\text{Zr}$ + $\text{ZrB}_2$ )+24 $\text{C}_f$	10	4.8
RMI-2				74( $\text{Zr}_2\text{Cu}$ + $\text{ZrB}_2$ )+20 $\text{C}_f$	6	5.4

Phases volumetric amounts and fibre contents were measured by image analysis on the polished surfaces of the samples where possible. Theoretical density values were calculated from these amounts, while geometric density was measured on the specimen bars. From the ratio of the experimental and theoretical density, relative density, and therefore porosity, were calculated. All the composites were machined to obtain at least 10 specimens for each composition. The microstructures were analysed by FESEM (FE-SEM, Carl Zeiss Sigma NTS GmbH Öberkochen, Germany) before and after thermal cycles. Oxidation treatments at 2278 K were carried out in an inductively-heated multipurpose furnace facility, called INDUTHERM, available at the German Aerospace Center (DLR, Stuttgart), Fig. 1. Ramping and isothermal dwelling were controlled via a two-colour pyrometer which directly commands the heating power unit. The hot chamber was completely lined with porous zirconia blankets: batches of up to six samples were carefully mounted on home-made porous zirconia setters, then two cycles of pumping down to about 1 mbar and Ar flushing up to an inner pressure of 0.6 mbar were completed before ramping up the temperature, at 100 K/min, to the target of 2278 K. The porous zirconia setters had the main function of holding the samples and preventing their interaction at these temperatures. During the temperature ramp the atmosphere was Ar at a pressure of 0.2 mbar, once the targeted temperature was reached, a gas inlet was opened and air started flowing at 5 l/min for 2 min (the filling time of the chamber was about 12 s); a couple of holes permitted the air to flow through and then exit from the opposite side of the chamber.

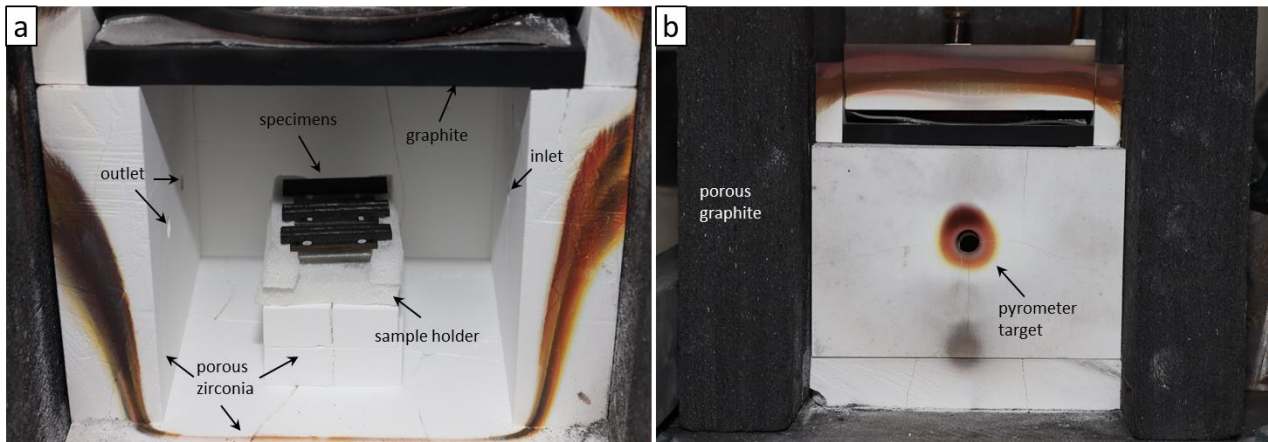


**Fig. 1.** INDUTHERM oxidation chamber: a) oxidation chamber constituted by porous zirconia walls, zirconia sample holder, inlet/outlet holes for gas, and a graphite susceptor as top cover. b) assembled chamber with the outside cover showing the hole targeted by the pyrometer.

Flexural strength ( $\sigma$ ) tests in a four-point bending configuration at room temperature were carried out following the guidelines of standard ISO 14704:2016 (EN) and using a fully-articulated steel fixture with a lower span of 20 mm and an upper span of 10 mm; the crosshead speed of a universal

testing machine (mod. Z050, ZwickRoell GmbH & Co. KG, Ulm-Einsingen, Germany) was 1 mm min<sup>-1</sup>. Due to the limitations in size of the produced materials, the preferred nominal dimensions of the specimens were 25 × 2.5 × 2.0 mm<sup>3</sup>. The machined specimens showed a dimensional variation lower than 0.1 mm (average 0.01 mm). No chamfering or rounding of the edges or mechanical surfaces treatments (e.g. polishing) were carried out. In the case of the CVI-based compositions, the specimens were machined with a width of 7 mm to ensure that they complied with the 2.5D fibre arrangement. At least three valid tests were performed for each kind of composite. The work of fracture (WoF) was calculated by integrating the area below the load/displacement curve divided by the double of the projected real surface.

### **3 Results and Discussion**

#### *3.1 Microstructure of as-produced composites*



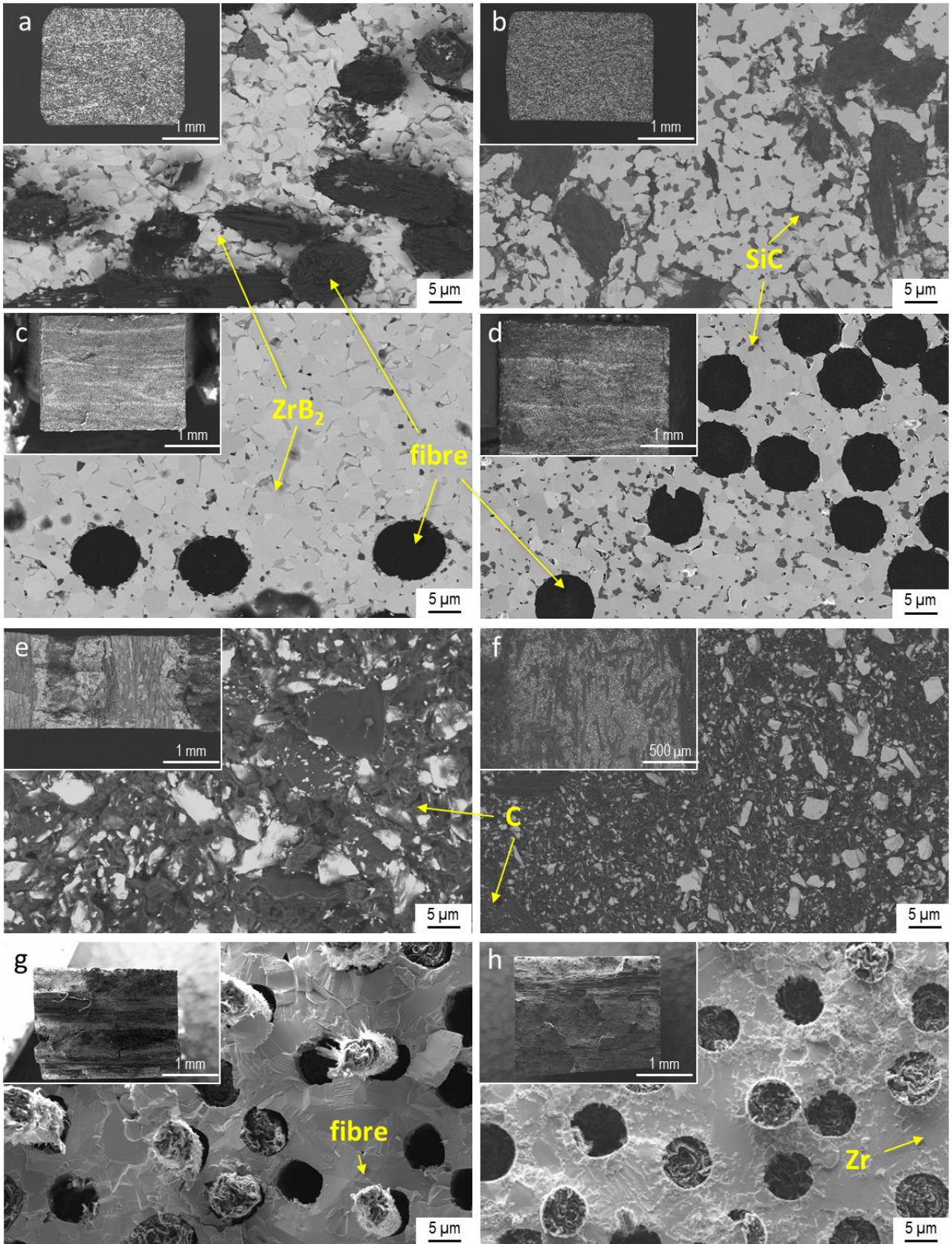


**Fig. 2.** Microstructure before oxidation of specimens: (a) CFHP and (b) MFSPS showing fibres (black), SiC (dark grey), ZrB<sub>2</sub> (light grey); (c) SIHP-1 and (d) SIHP-2 showing fibres (black), SiC (dark grey), ZrB<sub>2</sub> (light grey); (e) CVI-1 and (f) CVI-2 showing a dark matrix of carbon with white particles of UHTC phases; (g) RMI-1 and (h) RMI-2 showing fibres pull-out from the ceramic/metal matrix.

The different microstructure features are illustrated in Fig. 2 a-h and described below.

- *Sintered short fibre-reinforced ZrB<sub>2</sub>/SiC composites (CFHP, MFSPS)*. Both specimens displayed a fully dense microstructure with a similar random distribution of fibres (Fig. 2 a,b and insets) that were about 300 µm long for CFHP and 100 µm long for MFSPS. The SiC was homogeneously dispersed in the ZrB<sub>2</sub> matrix and the fibres were well anchored to the matrix. The fracture surface was rather smooth, indicating a strong adhesion with the matrix and limited fibre pull-out, Fig. 2 a. Both specimens contained 40 vol.% fibres, but sample MFSPS had a higher amount of SiC, as evident in Fig. 2 b.

- *Sintered continuous fibre-reinforced ZrB<sub>2</sub>/SiC composites (SIHP-1 and 2)*. This group of materials comprised two ZrB<sub>2</sub>/SiC composites with different SiC contents (5 and 10 vol.% respectively for SIHP-1 and SIHP-2). For both composites, the fibre volumetric content was overall higher than short fibre-reinforced composites (48 vs 40%), whilst a comparable full matrix densification was obtained for both specimens (Fig. 2 c,d insets). Fibres (black) and SiC (dark grey) were homogeneously distributed in the ZrB<sub>2</sub> matrix (light grey) and the fibre/matrix interface was very strong, as can be seen from the intimate contact between the fibres and the surrounding ceramic matrix (Fig. 2 c,d).

- *2.5D fibre-reinforced C/C-ZrB<sub>2</sub> composites fabricated via CVI (CVI-1 and 2)*. The third class of materials was constituted by 2.5D fibre-reinforced C/C composites doped with 20-30% ZrB<sub>2</sub> and produced via radio-frequency assisted chemical vapour infiltration. The microstructure of both specimens before testing is shown in Fig. 2 e,f. The complex 2.5D preform architecture is outlined in the insets of Fig. 2 e, f. The C<sub>f</sub>/C matrix is represented by the dark regions, while the white spots are ZrB<sub>2</sub> particles. The latter is more easily recognizable in Fig. 2 e as coarse white particles. For specimen CVI-2, the finer particle component was Y<sub>2</sub>O<sub>3</sub> (Fig. 2 f). Large pores were more evident in CVI-1 as black isolated spots in Fig. 2e, whilst sample CVI-2 specimens were characterized by a more dense carbon matrix. The lower density of the composite could be attributed to the presence of lighter phases such as SiC and Y<sub>2</sub>O<sub>3</sub>.

- *Continuous fibre-reinforced Zr/ZrB<sub>2</sub> composites fabricated via RMI (RMI-1 and 2)*. These composites were produced by reactive melt infiltration with slightly different procedures, as previously described. For specimen RMI-1, the molten Zr reacted with the boron source (provided by B<sub>4</sub>C) to produce in-situ ZrB<sub>2</sub> and ZrC, Fig. 2 g,h. Due to the similar contrast displayed by the constituent phases, a precise quantification of ZrB<sub>2</sub>, residual Zr and ZrC was not possible. The final fibre content amounted to ~25%, which was attributed to the swelling of the material during infiltration as previously observed by Vinci et al [25]. For specimen RMI-2, the Zr<sub>2</sub>Cu reacted with



B<sub>4</sub>C, resulting in the formation of ZrB<sub>2</sub>/ZrC phases, whilst the majority of residual copper segregated to the surface of the sample. In spite of the lower processing temperature, this sample displayed a higher degree of fibre degradation, suggesting that the Zr<sub>2</sub>Cu melt was much more reactive. Because of this, the final fibre content was even lower than RMI-1, amounting to ~20 vol.%. Both specimens were characterized by little or no fibre pull-out. As in the previous work [25], the shrinkage of the metallic phase during cooling led to the fibre/matrix debonding, i.e. a weak interface was formed. In fact, looking at fracture surfaces showed in Fig. 2, it was observed that matrix around fibres was actually detached from the fibre and the perception is that fibre failures close to the crack plane occurred in the crack tip rather than in the crack wake.

### *3.2 Microstructure after thermal treatment*

Thermal treatment at 2278K / 2 min in air led to strong oxidation phenomena. In the absence of any environmental coating, the exposed surfaces underwent C<sub>f</sub> and carbon phase burnout that left large pores and oxidation of the matrix phases (ZrB<sub>2</sub>, SiC), whilst any metallic phases melted. Features of the oxidised samples are illustrated in Fig. 3 (a-h).

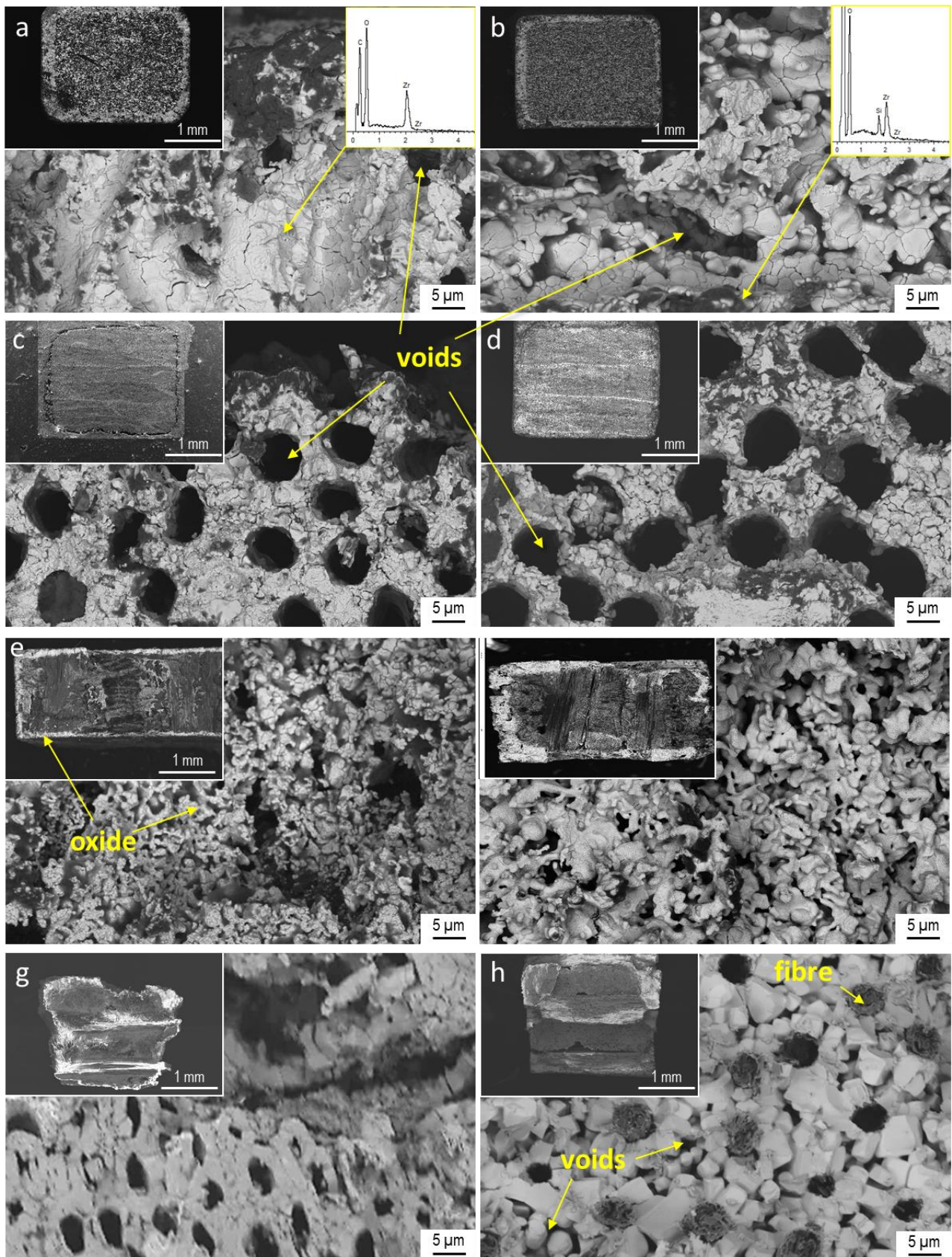


**Fig. 3.** Microstructure of specimens after oxidation: (a) CFHP and (b) MFSPS: morphology of the  $\text{ZrO}_2$  scale and inset of the EDS spectra (carbon signal comes from the conductive carbon coating); (c) SIHP-1 and (d) SIHP-2: morphology of the  $\text{ZrO}_2$  scale and the hollows left by the fibre oxidation; (e) CVI-1 and (f) CVI-2: morphology of the oxidised layer, showing larger  $\text{ZrO}_2$  grains for CVI-2, (g) RMI-1 and (h) RMI-2 showing

the inhomogeneous oxidation which affected even the bulk material, with the partial loss of the metallic phase.

- *Sintered short fibre-reinforced  $ZrB_2/SiC$  composites (CFHP, MFSPS).* After heat treatment at 2278 K in severely oxidizing conditions, CFHP and MFSPS were characterized by the homogeneous oxidation of the outer layer that was mainly characterized by an outer  $ZrO_2$  scale and an inner  $ZrO_2/SiO_2$  layer, Fig. 3 a, b insets. Oxidation of the carbon fibres in the outer layers left holes in the zirconia scale that were only partially filled with silica. The thickness of the oxide layer observed in CFHP,  $\sim 170\ \mu m$ , was slightly higher than for MFSPS,  $\sim 140\ \mu m$ , and this was attributed to the slightly different porosity and SiC content. In both cases the porous nature of the oxide scale produced a brittle layer, Fig. 3 a,b.

- *Sintered continuous fibre  $ZrB_2/SiC$  composites (SIHP-1, 2).* Just as observed for the short fibre-reinforced UHTCs, samples SIHP-1 and SIHP-2 were also characterized by the homogeneous oxidation of the outer layer, insets in Fig. 3 c, d, with the formation of an outer  $ZrO_2$  layer and an intermediate porous layer of  $ZrO_2$  and some traces of  $SiO_2$  and the hollows left by the fibre removal, Fig. 3 c, d. Specimen SIHP-1 was characterized by a weaker oxide scale, as evidenced by its tendency to detach from the bulk material, Fig. 3 c. This was attributed to the lower amount of SiC that, during oxidation, provides a source of liquid phase that holds the  $ZrO_2$  grains together. The thickness of the oxide layers was  $\sim 100\ \mu m$  and  $\sim 80\ \mu m$  for SIHP-1 and SIHP-2 respectively, which was lower than for the short fibre-reinforced composites. However, since the oxide layer was quite brittle and prone to detachment from the bulk surface unlike short fibre-reinforced composites, it is believed that the oxidised cross section did not contribute to the mechanical resistance during testing.

- *2.5D fibre-reinforced C/C- $ZrB_2$  composites fabricated via CVI (CVI-1, 2).* The microstructure of specimens CVI-1 and CVI-2 after heat treatment is shown in Fig. 3, e,f. Both specimens were characterized by the formation of an outer layer of porous  $ZrO_2$ , which in the case of CVI-2 displayed a particular morphology due to the presence of  $Y_2O_3$ , Fig. 3 f. Specimen CVI-2 had a consistently thicker oxide scale,  $\sim 200\ \mu m$ , Fig. 3 f-inset, compared to CVI-1,  $\sim 120\ \mu m$ , which could be attributed both to the overall lower content of the UHTC and to the layer configuration. Another reason could be attributed to the partial loss of material during machining which might have created further paths for oxygen diffusion.

- *Continuous fibre-reinforced  $Zr/ZrB_2$  composites fabricated via RMI.* The samples produced by RMI were the most affected by the heat treatment. Beside the carbon fibre burnout, the presence of residual unreacted metals with melting point lower than the heat treatment temperature led to the

matrix collapse. Another phenomenon that might have contributed to the matrix collapse is the volume expansion resulting from the oxidation of the residual metal. Both specimens were characterized by a high degree of oxidation that reached even the interior of the material, Fig. 3 g, h insets. RMI-1 was characterized by the hollows left by the fibre oxidation and by the formation of an inhomogeneous layer of  $\text{ZrO}_2$  surrounded by the leftover alloy, Fig. 3 g. In the case of RMI-2, even the internal microstructure was affected, with the loss of the leftover Cu-based alloy that at 2278 K was rapidly removed, leaving a highly porous internal microstructure made up almost entirely of  $\text{ZrC}$  and residual  $\text{Zr}$ , Fig. 3 h.

### 3.3 Flexural strength

The values of flexural strength and stress-displacement curve of as-produced samples are reported in Fig. 4 and Fig. 5, respectively. For the sake of comparison, these figures also show the situation after oxidation at 2278 K. The right-hand ordinate of Fig. 4 a shows the specific strength of as produced composites.

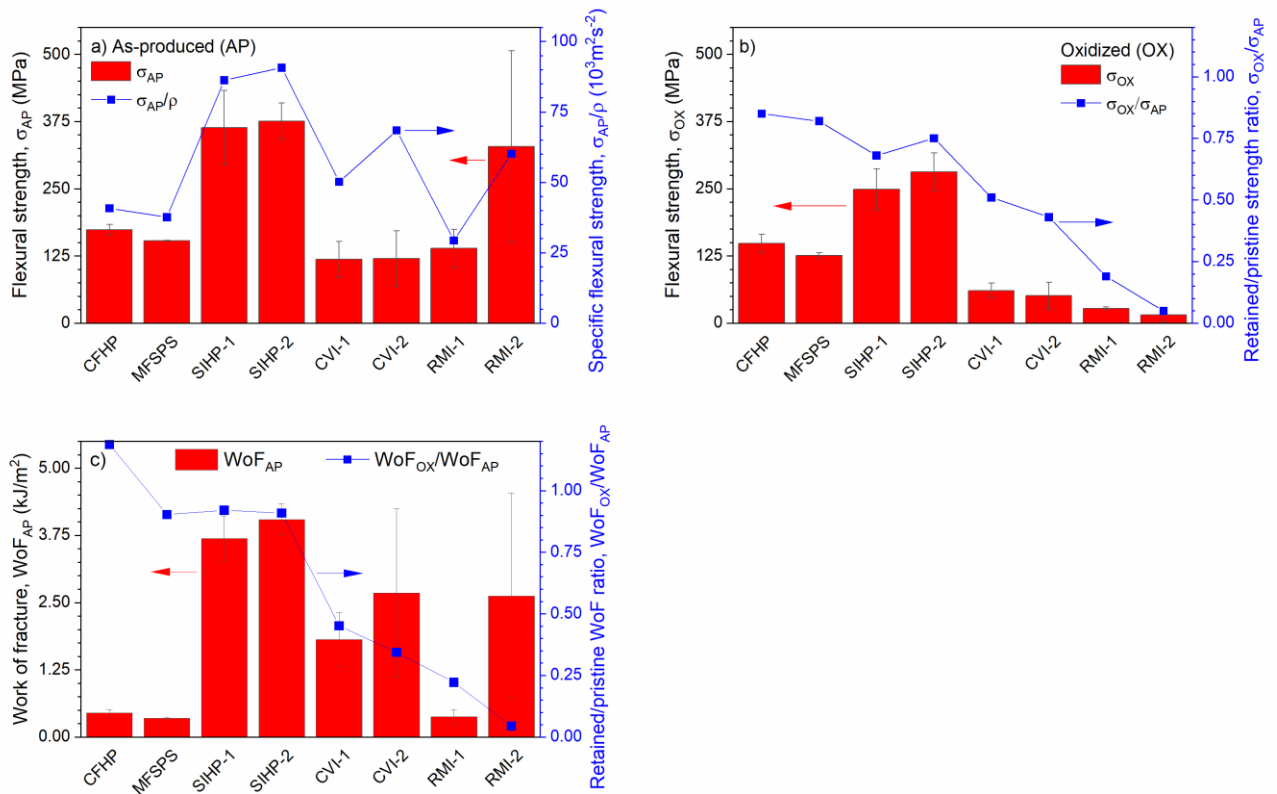


**Fig. 4.** a) Flexural strength (bars) of as-produced composites. The right-hand ordinate refers to the specific flexural strength (filled symbols). b) Flexural strength (bars) of composites after oxidation. The right-hand ordinate refers to the retained/pristine strength ratio (filled symbols). c) Work of fracture (bar) of as-produced composites. The right-hand ordinate refers to the retained/pristine ratio of WoF

(filled symbols).

- *Pristine flexural strength.* As expected, there is plenty of difference in the mechanical responses among the UHTCMCs, due to the different composites, type of fibre and fibre arrangements. For the same reason, also a direct comparison with the literature is not easy. However, the obtained flexural strength values are within the range of values reported in the literature [15]. The highest values, 350 MPa, were obtained for composites with no porosity and unidirectional fibres, SIHP-1, SIHP-2 and for the RMI samples. Strength of 150-170 MPa were found for the random chopped fibre-reinforced composites and 120-150 MPa for CVI samples, which had a 2.5D fibre preform arrangement. The degree of scatter around the mean values is also indicative of the different microstructural features. The random short fibre-reinforced samples were very homogenous, whilst increasing the complexity of the arrangement also increased the variability in the strength values. The load displacement curves of the as-produced materials also revealed other interesting features. The short fibre-reinforced composites, Fig. 5 a and b, as well as the continuous fibre-reinforced composites produced by RMI, Fig. 5 g and h, showed a predominantly brittle failure. In the short-fibre composites, this was due to the reduced fibre dimensions (100-300  $\mu\text{m}$ ) and dense matrix. In the RMI composites, the matrix-dominated behaviour was ascribed to the dense matrix and to the relatively low fibre volume content, <30 vol.%. The reaction of the molten alloy with the uncoated fibres also jeopardized the flexural strength, which displayed a large data scatter, Fig.4 a. On the other hand, the SIHP and CVI samples displayed damage tolerant behaviour, with flexural test curves similar to other CMCs, Fig. 5 c-f, thanks to the high fibre content and weak matrix / fibre interface, respectively. The three-stage deformation before fracture showed in the stress-displacement curves of SIHP-1 and SIHP-2 could be justified with the ACK model [26], although there is some discrepancy between the experimental curve and the theoretical ones. In particular, the stiffness recovery in the last stage, that in some case overcome the pristine value, is not foreseen by the ACK model. This behaviour is not still understood and is ascribed to the improvement of the



fibres alignment allowed by the formation of the so called inner freed fibres (IFF) after the matrix cracking and the local releasing of the residual compressive strain of the fibres [21].

The above considerations about the failure behaviour (brittle or non-brittle) are in agreement with the calculated WoF (Fig. 4 c). The MFSPS specimens showed the lowest value of  $0.35 \text{ kJ/m}^2$ . The WoF slightly increases, up to  $0.45 \text{ kJ/m}^2$ , in the case of FDHP specimens. This value is comparable with that showed by continuous fibre-reinforced UHTCMC characterized by strong fibre/matrix interfaces [27]. On the other hand, the highest value of about  $4 \text{ kJ/m}^2$  corresponds to the SIHP specimens. This value approaches the upper limit of  $4.6 \pm 1.2 \text{ kJ/m}^2$  showed by continuous fibre-reinforced UHTCMC characterized by weak fibre/matrix interfaces [27]. The RFCVI specimens, having a WoF between  $1.8$  and  $2.7 \text{ kJ/m}^2$ , showed an energy dissipation to the fracture higher than those reported in literature, generally lower than  $2 \text{ kJ/m}^2$  [28]. As with flexural strength, the RMI-1 specimens with a WoF of  $0.38 \text{ kJ/m}^2$  confirm their brittle behaviour, while the large data scatter of RMI-2 ( $\text{WoF} = 2.6 \pm 1.9 \text{ kJ/m}^2$ ) confirms the not perfectly controlled reaction of the molten alloy with the fibres.



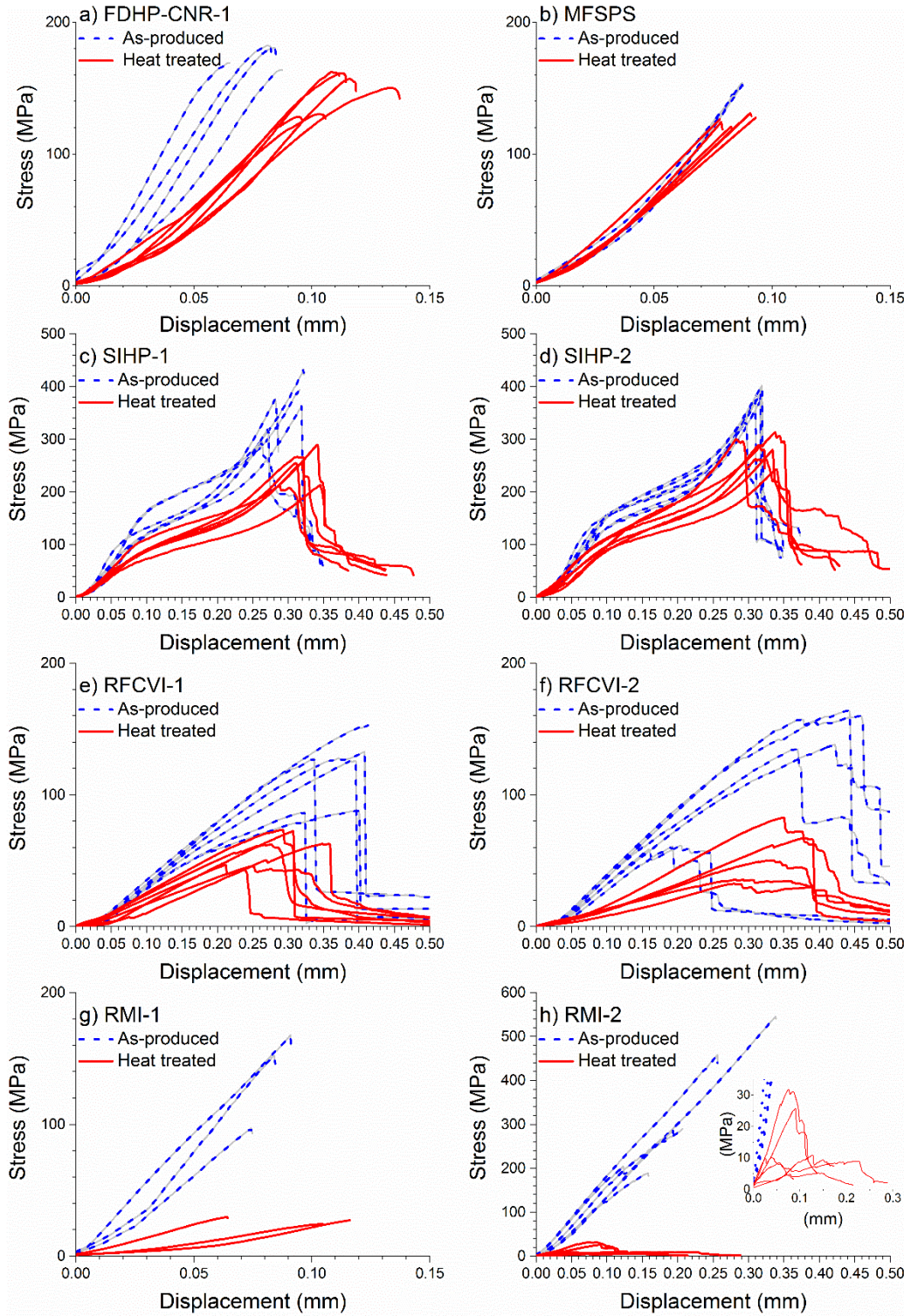


**Fig. 5.** Stress-displacement curves of as-produced (dotted curves) and heat treated at 2278 K (solid curves) specimens: a) chopped fibre dispersion and hot-pressing sintered UHTC (CFHP); b) milled short fibre dispersion and spark plasma sintered UHTC (MFSPS); c, d) 0/0° continuous carbon fibre-reinforced UHTC by slurry infiltration and sintering by hot-pressing (SIHP); e, f) 2.5D ultra-high temperature ceramic matrix composites by chemical vapor infiltration (CVI-1) and RF heated chemical vapour infiltration (CVI-2); g, h) 0/90° continuous carbon fibre-reinforced UHTC by reactive melt infiltration (RMI). h-inset) zoom of the curves of the heat treated RMI-2 samples.

- *Retained flexural strength after heat treatment at 2278 K.* Values and curves of strength after sample oxidation are reported in Fig. 4 b and 5. The right-hand ordinate of Fig. 4 b shows the retained / initial strength ratio. In all cases, the failure mode, brittle or non-brittle, did not change within each class of composite, see Fig. 5. On the contrary, the slope of the curves showed a notable variation, indicating a marked change in the modulus. The loss of strength was related to the effects of oxidation at 2278 K inducing a significant level of damage at the surface. Assuming that for most of the samples the bulk damage was less important, the formation of a compact and dense oxide resulted in minimum variation of the strength. On the contrary, a highly damaged external layer severely impacted the strength.

Fig. 5 shows that both types of short fibre-reinforced composites, CFHP and MFSPS, maintained the highest values of retained strength, above 80% of the initial values. This was attributed to the higher amount of protective ceramic matrix (60 vol.%) surrounding the carbon fibres and the very low amount of residual porosity, which was <1 vol.%. Since the internal microstructure was apparently unchanged, the resulting decrease in strength can be simply attributed to the smaller cross section under loading and the lower strength contribution provided by the oxide scale. In the case of the MFSPS, the limited oxidized layer allowed the stiffness to be retained, as demonstrated by the overlapping nature of the curves of the as-produced and thermally treated specimens, Fig. 5 b. However, looking more deeply the load-displacement curve, the higher displacement to failure showed by the heat treated CFHP specimens suggests a weakening of the matrix/fibre interfaces, which may explain the 18% increase in WoF after heat treatment (Fig. 4 c).

For sintered composites with continuous fibres, SIHP-1 and 2, their retained strength and WoF decreased to around 70% and 90%, respectively, of the unoxidised values. In this case, the higher amount of carbon fibres, 47-48%, left large empty channels in the scale, increasing the rate of oxidation and making the scale more brittle. The CVI samples retained 35-45 % of their original WoF and 40-50 % of their original strength, which was attributed to the original residual porosity, higher than 10%, and the high amount of carbon phase originally present, both in the form of fibre and pyrolytic carbon, both of which will have burnt out leading to an increase in the oxidation kinetics. Finally, the RMI composites showed the lowest retained strength and WoF, below 20%. This result was expected because the heat treatment at 2278 K strongly damaged the matrix down to the centre of the cross section, leaving a discontinuous microstructure.

## 4 Conclusions

For the first time, the flexural strength of different types of UHTCMCs has been compared before

and after oxidation at 2278 K in air. All the composites were damaged to some extent by the oxidation of the most vulnerable phase, the C, which led to the formation of pores and channels and hampered the formation of a fully protective oxide scale. The short fibre-reinforced composites showed the best oxidation resistance and a retained strength higher than 80% of its original value thanks to the dense matrix and the limited amount of fibres present (40 vol.%). The continuous fibre-reinforced composites, which were characterized by 50 vol.% of fibre and a dense UHTC matrix, maintained ~70% of their original strength. With an increase in the amount of carbon phase present, the RF-CVI-based samples, the retained strength decreased down to ~50%. Nevertheless, all UHTCMCs with a ZrB<sub>2</sub>-based ceramic matrix demonstrated the ability to sustain extreme temperatures in an air environment with a promising degree of strength retention. In contrast, the UHTCMCs processed by the RMI technique were found to be unsuitable for application at such a high temperature, due to the presence of unreacted residual metal that led to a severe loss of matrix stability. [Future works will be focused on the ablation resistance of the first two classes of materials that showed the highest strength retention.](#)

## Acknowledgements

This work has received funding from the European Union's Horizon 2020 "Research and innovation programme" under grant agreement No 685594 (C<sup>3</sup>HARME). The authors wish to thank Cesare Melandri and Federico Saraga for technical support.

## References

- [1] Sciti D, Silvestroni L, Monteverde F, Vinci A, Zoli L. Introduction to H2020 project C3HARME—next generation ceramic composites for combustion harsh environment and space. *Adv Appl Ceram* 2018. doi:10.1080/17436753.2018.1509822.
- [2] Zoli L, Sciti D, Vinci A, Galizia P, Monteverde F, Failla S, et al. *Ultra-High Temperature Ceramic Matrix Composites*, Elsevier; 2020. doi:https://doi.org/10.1016/B978-0-12-818542-1.00023-0.
- [3] Wang Y, Chen Z, Yu S. Ablation behavior and mechanism analysis of C / SiC composites. *J Mater Res Technol* 2015;5:170–82. doi:10.1016/j.jmrt.2015.10.004.
- [4] Zhang D, Hu P, Dong S, Liu X, Wang C, Zhang Z, et al. Oxidation behavior and ablation mechanism of Cf/ZrB<sub>2</sub>-SiC composite fabricated by vibration-assisted slurry impregnation combined with low-temperature hot pressing. *Corros Sci* 2019;161:108181. doi:10.1016/j.corsci.2019.108181.
- [5] Ouyang H, Zhang Y, Li C, Li G, Huang J, Li H. Effects of ZrC/SiC ratios on mechanical and

ablation behavior of C/C–ZrC–SiC composites prepared by carbothermal reaction of hydrothermal co-deposited oxides. *Corros Sci* 2019;163:108239. doi:10.1016/j.corsci.2019.108239.

- [6] Rueschhoff LM, Carney CM, Apostolov ZD, Cinibulk MK. Processing of fiber-reinforced ultra-high temperature ceramic composites: A review. *Int J Ceram Eng Sci* 2020;2:22–37. doi:10.1002/ces2.10033.
- [7] Chen BW, Ni DW, Liao CJ, Jiang YL, Lu J, Dong SM. Long-term ablation behavior and mechanisms of 2D-Cf/ZrB<sub>2</sub>-SiC composites at temperatures up to 2400 °C. *Corros Sci* 2020;177:108967. doi:10.1016/j.corsci.2020.108967.
- [8] Chen X, Feng Q, Zhou H, Dong S, Wang J, Cao Y, et al. Ablation behavior of three-dimensional Cf/SiC-ZrC-ZrB<sub>2</sub> composites prepared by a joint process of sol-gel and reactive melt infiltration. *Corros Sci* 2018;134:49–56. doi:10.1016/j.corsci.2018.02.011.
- [9] Huang D, Zhang M, Huang Q, Wang L, Xue L, Tang X, et al. Ablation mechanism of C/C-ZrB<sub>2</sub>-ZrC-SiC composite fabricated by polymer infiltration and pyrolysis with preform of Cf/ZrB<sub>2</sub>. *Corros Sci* 2015;98:551–9. doi:10.1016/j.corsci.2015.05.064.
- [10] Zhuang L, Fu QG, Liu TY. Ablation resistance of wedge-shaped C/C-ZrB<sub>2</sub>-ZrC-SiC composites exposed to an oxyacetylene torch. *Corros Sci* 2016;112:462–70. doi:10.1016/j.corsci.2016.08.010.
- [11] Hu C, Pang S, Tang S, Wang S, Huang H, Cheng HM. Ablation and mechanical behavior of a sandwich-structured composite with an inner layer of Cf/SiC between two outer layers of Cf/SiC-ZrB<sub>2</sub>-ZrC. *Corros Sci* 2014;80:154–63. doi:10.1016/j.corsci.2013.11.019.
- [12] Tang S, Deng J, Wang S, Liu W. Comparison of thermal and ablation behaviors of C/SiC composites and C/ZrB<sub>2</sub>-SiC composites. *Corros Sci* 2009;51:54–61. doi:10.1016/j.corsci.2008.09.037.
- [13] Hald H. Operational limits for reusable space transportation systems due to physical boundaries of C/SiC materials. *Aerosp Sci Technol* 2003;7:551–9. doi:10.1016/S1270-9638(03)00054-3.
- [14] Wang X, Wei K, Tao Y, Yang X, Zhou H, He R, et al. Thermal protection system integrating graded insulation materials and multilayer ceramic matrix composite cellular sandwich panels. *Compos Struct* 2019;209:523–34. doi:10.1016/J.COMPSTRUCT.2018.11.004.
- [15] Binner J, Porter M, Baker B, Zou J, Venkatachalam V, Diaz VR, et al. Selection, processing, properties and applications of ultra-high temperature ceramic matrix composites, UHTCMCs – a review. *Int Mater Rev* 2019. doi:10.1080/09506608.2019.1652006.
- [16] Zhang D, Feng J, Hu P, Xun L, Liu M, Dong S, et al. Enhanced mechanical properties and



thermal shock resistance of Cf/ZrB<sub>2</sub>-SiC composite via an efficient slurry injection combined with vibration-assisted vacuum infiltration. *J Eur Ceram Soc* 2020. doi:10.1016/j.jeurceramsoc.2020.07.003.

- [17] Hu P, Cheng Y, Zhang D, Xun L, Liu M, Zhang C, et al. From ferroconcrete to Cf/UHTC-SiC: A totally novel densification method and mechanism at 1300 °C without pressure. *Compos Part B Eng* 2019;174:107023. doi:10.1016/j.compositesb.2019.107023.
- [18] Liu Y, Zu Y, Tian H, Dai J, Sha J. Microstructure and mechanical properties of continuous carbon fiber-reinforced ZrB<sub>2</sub>-based composites via combined electrophoretic deposition and sintering. *J Eur Ceram Soc* 2020. doi:10.1016/j.jeurceramsoc.2020.10.044.
- [19] Vinci A, Zoli L, Sciti D, Watts J, Hilmas GE, Fahrenholtz WG. Mechanical behaviour of carbon fibre reinforced TaC/SiC and ZrC/SiC composites up to 2100°C. *J Eur Ceram Soc* 2018;39:780–7. doi:10.1016/J.JEUCERAMSOC.2018.11.017.
- [20] Galizia P, Zoli L, Sciti D. Impact of residual stress on thermal damage accumulation, and Young's modulus of fiber-reinforced ultra-high temperature ceramics. *Mater Des* 2018;160:803–9. doi:https://doi.org/10.1016/j.matdes.2018.10.019.
- [21] Galizia P, Sciti D, Saraga F, Zoli L. Off-axis damage tolerance of fiber-reinforced composites for aerospace systems. *J Eur Ceram Soc* 2020;40:2691–8. doi:10.1016/j.jeurceramsoc.2019.12.038.
- [22] Cheng T. Understanding the ultra-high-temperature mechanical behaviors of advanced two-dimensional carbon-carbon composites. *Ceram Int* 2020. doi:10.1016/j.ceramint.2020.05.237.
- [23] Li L. Modeling Temperature-Dependent Vibration Damping in C/SiC Fiber-Reinforced Ceramic-Matrix Composites. *Materials (Basel)* 2020;13:1633. doi:10.3390/ma13071633.
- [24] Baker B, Rubio V, Ramanujam P, Binner J, Hussain A, Ackerman T, et al. Development of a slurry injection technique for continuous fibre ultra-high temperature ceramic matrix composites. *J Eur Ceram Soc* 2019;39:3927–37. doi:10.1016/j.jeurceramsoc.2019.05.070.
- [25] Vinci A, Zoli L, Galizia P, Küttemeyer M, Koch D, Sciti D. Reactive melt infiltration of carbon fibre reinforced ZrB<sub>2</sub>/B composites with Zr<sub>2</sub>Cu. *Compos Part A Appl Sci Manuf* 2020. doi:10.1016/j.compositesa.2020.105973.
- [26] Aveston J, Kelly A. Theory of multiple fracture of fibrous composites. *J Mater Sci* 1973; 8:352-362. doi:10.1007/BF00550155
- [27] Sciti D, Zoli L, Vinci A, Silvestroni L, Mungiguerra S, Galizia P. Effect of PAN-based and pitch-based carbon fibres on microstructure and properties of continuous Cf/ZrB<sub>2</sub>-SiC UHTCMCs. *J Eur Ceram Soc* 2020;41:3045–50. doi:10.1016/j.jeurceramsoc.2020.05.032.

- [28] Zhang D, Hu P, Dong S, Qu Q, Zhang X. Effect of pyrolytic carbon coating on the microstructure and fracture behavior of the Cf/ZrB<sub>2</sub>-SiC composite. *Ceram Int* 2018;44:19612–8. doi:10.1016/J.CERAMINT.2018.07.210.